

Radio Spectral Energy Distribution of Low- z Metal Poor Extreme Starburst Galaxies:

Novel insights on the escape of ionizing photons

Omkar Bait^{1,2,*}, Daniel Schaerer^{1,3}, Yuri I. Izotov⁴, and Biny Sebastian⁵

¹ Observatoire de Genève, Université de Genève, Chemin Pegasi, 1290 Versoix, Switzerland
e-mail: omkar.bait@unige.ch

² SKA Observatory, Jodrell Bank, Lower Withington, Macclesfield, SK11 9FT, UK
e-mail: omkar.bait@skao.int

³ CNRS, IRAP, 14 Avenue E. Belin, 31400 Toulouse, France

⁴ Bogolyubov Institute for Theoretical Physics, 14-b Metrolohichna str, Kyiv 03143, Ukraine

⁵ Space Telescope Science Institute, 3700 San Martin Drive, Baltimore, MD 21218, USA

Received; accepted

ABSTRACT

Context. Recent optical surveys have found a rare population of low- z ($z \sim 0.01 - 0.06$) extreme star-forming galaxies (xSFGs) that are the most metal-poor galaxies with strong emission lines, extremely high specific star-formation rate and low stellar mass. Using the Hubble Space Telescope Cosmic Origins Spectrograph, it was found that xSFGs are strong Ly α emitters (LAEs). Their Ly α properties indirectly suggest that they are also strong LyC leakers. This along with several other global properties makes them similar to the recently found $z > 6$ reionization-era star-forming galaxies using the James Webb Space Telescope.

Aims. Here we aim to study the radio spectral energy distribution (radio-SED) of 8 xSFGs to understand mechanisms behind the extreme nature of star-formation in these galaxies, particularly their high ionisation state and possible strong LyC leakage. Using radio-SED analysis we can constrain the thermal/non-thermal fraction which allows us to study the role of supernova and cosmic-ray feedback in driving the extreme nature of xSFGs and also constrain the density of the interstellar medium (ISM). The radio thermal emission can also be used to study the presence of dust, particularly that which could be missing in the optical.

Methods. We present new multi-frequency radio continuum (RC) observations using a combination of upgraded Giant Metrewave Radio Telescope (uGMRT), the Karl G. Jansky Very Large Array (VLA) together with archival LOw Frequency ARray (LOFAR) survey data for a few sources. We performed RC observations using the uGMRT at Band-5 (1060 – 1460 MHz) together with VLA S- (2 – 4 GHz), C- (4 – 8 GHz), X- (8 – 12 GHz) and Ku- (12 – 18 GHz) bands. The VLA S- and C-band observations were performed in B-configuration, whereas the X- and Ku-band observations were performed in C-configuration. Such a multi-configuration setup allows us to study the radio-SED in a roughly spatially matched resolution of $3 \sim 2''$. For a few sources we also present LOFAR 120-168 MHz observations at $6''$ resolution. Using these RC observations, we map the radio-SED of 8 xSFGs in a wide frequency range from ~ 1 GHz (from 150 MHz for a few sources) - 15 GHz, up to ~ 2 orders of magnitude in frequency.

Results. The radio-SED of xSFGs is flat between 6-15 GHz and shows a strong evidence for a turnover at lower frequencies in the range of 2 – 10 GHz. They can be well described using a thermally dominated radio spectra with a free-free absorption component with a high emission measure. Thus the star-forming complexes in these galaxies are extremely young (pre-SNe stage; below ~ 5 Myrs) and the interstellar medium is very dense. This, along with the overall shape of the radio-SED, suggests a dominance of young massive star clusters (YMCs) in these galaxies. One source, J150934+373146, is an exception to this trend and instead has a steep spectrum below 10 GHz and shows a break at higher frequencies. A comparison between the radio free-free emission at 10 GHz with that observed from the $H\beta$ emission line in the optical provides evidence of dust in several xSFGs. In a few cases there is evidence for a small fraction of the ionizing emission of the galaxy being not visible in the Balmer lines, which is possibly due to being deeply embedded in YMCs. We confirm previously found dependence between Lyman continuum escape fraction ($f_{\text{esc}}^{\text{LyC}}$), ionisation state and the radio spectral index, particularly for strong leakers.

Conclusions. Our radio-SED analysis suggests that a dominance of YMCs in metal poor extreme starburst galaxies leads to their several extreme star-forming properties along with potentially leaking a significant amount of hydrogen ionising photons.

Key words. galaxies: starburst – Radio continuum: galaxies – Radio continuum: ISM

1. Introduction

Identifying the nature of sources (at redshift $z > 6$) that led to the reionization of the Universe remains a matter of intense debate. Numerous studies, both on the observational and simulation side, suggest that low-mass dwarf starburst galaxies are

likely the dominant sources of reionization (e.g., Ouchi et al. 2009; Bouwens et al. 2015; Robertson et al. 2015; Atek et al. 2015). With the advent of the James Webb Space Telescope (JWST), rest-frame optical spectroscopic studies of reionization-era galaxies ($z \sim 6 - 8$) have become possible revealing their key physical properties. It is found that these galaxies generally have low stellar masses ($\log M_*/M_\odot \leq 9$), compact size (< 1

* O. Bait is the corresponding author

kpc), and high specific star-formation rates sSFR of $\sim 100 \text{ Gyr}^{-1}$ (Schaerer et al. 2022; Rhoads et al. 2023; Williams et al. 2023; Endsley et al. 2023; Fujimoto et al. 2023; Mascia et al. 2024). Several of these galaxies are extremely metal-poor (XMPs), with gas-phase metallicities $12 + \log \text{O}/\text{H} < 8.0$ and have hard ionizing radiation (Jones et al. 2020; Schaerer et al. 2022; Rhoads et al. 2023; Langeroodi et al. 2023; Topping et al. 2024; Saxena et al. 2024; Atek et al. 2024). And importantly, they are found to be strong Ly α emitters (LAEs) and also produce a significant amount of ionizing radiation to easily reionize the Universe (Simmonds et al. 2023, 2024; Saxena et al. 2024; Atek et al. 2024).

Despite these significant advances in our understanding of high- z galaxies, the physical mechanisms responsible for their extreme star-forming properties and high LyC escape responsible for reionization remain poorly understood due to a lack of multi-wavelength studies, which is extremely difficult with the current generation telescopes. Moreover, due to optically thick inter-galactic medium it is extremely difficult to detect LyC escape from high- z galaxies (Inoue et al. 2014). We thus have to rely on the local analogs of such high- z galaxies with similar physical properties, e.g., low-mass, compact sizes, high sSFR, low-metallicity and strong Ly α emission etc. (e.g., Cardamone et al. 2009; Yang et al. 2017; Izotov et al. 2011, 2021a), generally found in the Sloan Digital Sky Survey (SDSS) data. These low- z ($z \sim 0.3$) analogs are known to produce a significant amount of LyC photons (Schaerer et al. 2016; Izotov et al. 2021a) and importantly a large fraction of them leak (Borthakur et al. 2014; Izotov et al. 2016c,a, 2018a,b, 2021b). These successes in finding local LyC leakers or emitters (LCEs) have led to the recent systematic study of the Low- z Lyman Continuum Survey (LzLCS; Flury et al. 2022a) which has revealed interesting relations between the LyC escape fraction ($f_{\text{esc}}^{\text{LyC}}$) and several key galaxy physical properties (Flury et al. 2022b; Saldana-Lopez et al. 2022; Xu et al. 2023; Jaskot et al. 2024; Bait et al. 2024).

Recently, a rare population of extreme star-forming galaxies (xSFGs) were discovered with the SDSS which are very compact XMPs having even lower stellar mass ($\log M_*/M_\odot \sim 5-8$), high sSFRs ($\sim 300 \text{ Gyr}^{-1}$) and high [OIII] $\lambda 5007$ /[OII] $\lambda 3727$ ratios; $\text{O}_{32} \geq 5$, with several in the range of 20-50 (Izotov et al. 2017b, 2020, 2024; Jaskot et al. 2019). They show diverse Ly α properties with several sources showing narrow Ly α peak velocity separation (V_{sep}) (Izotov et al. 2020, 2024). Such a narrow V_{sep} suggests that they are also strong LyC leakers based on the tight relation between V_{sep} and $f_{\text{esc}}^{\text{LyC}}$ (Verhamme et al. 2015; Izotov et al. 2018b). Here we focus on the multi-frequency radio continuum (RC) observations of xSFGs to gain new insights on the physical mechanisms driving their extreme SF and potentially strong $f_{\text{esc}}^{\text{LyC}}$.

RC emission from galaxies in the megahertz (MHz)- to gigahertz (GHz) frequency range has provided important insights on the star-formation process (Condon 1992). RC emission has been found to be an excellent tracer of extinction-free star-formation rate (SFR) in galaxies (e.g., Murphy et al. 2011, and references therein). The RC emission in normal SF galaxies consists of a combination of a flat thermal emission component (free-free emission with a spectral index of -0.1) and a non-thermal emission component (non-thermal spectral index $\alpha_{\text{nth}} \sim -0.8$). The non-thermal component arises from synchrotron emission from cosmic-ray particles (CRs) accelerated by supernova (SNe) under magnetic fields. Thus the non-thermal emission can be used to infer the SNe rate, cosmic-ray (CR) energy distribution and the equipartition magnetic fields. The radio

spectral energy distribution (radio-SED) of normal SF galaxies shows a power-law behaviour due to a combination of the thermal and non-thermal component. It is generally found that at $\sim 1.4 \text{ GHz}$ the non-thermal component is dominant comprising of almost 90% of the emission component (e.g., Niklas et al. 1997; Tabatabaei et al. 2017). Detailed multi-frequency radio-SED analysis of nearby SF galaxies has allowed to constrain the relative fraction of thermal ($f_{1\text{GHz}}^{\text{th}}$) and non-thermal emission, and α_{nth} (Tabatabaei et al. 2017) and its dependence on various galaxy physical parameters (e.g., the SFR surface density, magnetic fields etc.). Additionally in luminous and ultra-luminous infrared galaxies (ULIRGs), there can be a turnover at lower frequencies in the radio-SED due to free-free absorption (FFA) effects (e.g. Clemens et al. 2010; Galvin et al. 2018). Using a combination of thermal and non-thermal radio emission and FFA model, these studies find a high emission measure (EM) in ULIRGs in the range of $\sim 10^6 - 10^7 \text{ pc cm}^{-6}$ (Clemens et al. 2010; Galvin et al. 2018; Dey et al. 2024).

RC studies of dwarf galaxies have revealed different properties compared to massive SF galaxies. The thermal fraction ($f_{1\text{GHz}}^{\text{th}}$) is higher in dwarf galaxies, particularly in blue compact dwarfs (Klein et al. 1991; Deeg et al. 1993; Thuan et al. 2004; Ramya et al. 2011). A radio-SED study of nearby dwarf galaxies from $\sim 0.3 - 24 \text{ GHz}$ have shown that they cannot be described by a single power-law and instead show a cutoff/break at higher frequencies due to various physical processes related to the lack of CRs (Klein et al. 2018). More relevant to our study here, for example in an extremely metal-poor compact dwarf starburst, SBS 0335-052, the integrated radio-SED shows a strong turnover at GHz frequencies, arising due to FFA with a EM $\sim 2-8 \times 10^7 \text{ pc cm}^{-6}$ and compact size ($\sim 17 \text{ pc}$) (Hunt et al. 2004, hereafter: H04). Such a high EM is more commonly observed in resolved radio studies of ultra dense HII regions comprising of young deeply embedded star clusters (e.g., Kobulnicky & Johnson 1999; Johnson & Kobulnicky 2003). Previous single frequency (at 1.4 GHz and 150 MHz) RC observations of objects similar to xSFGs (e.g., green-peas, blueberries) have found that these systems have lower RC flux than that expected from the standard RC-SFR relation (Chakraborti et al. 2012; Sebastian & Bait 2019; Borkar et al. 2024). However, due to limited frequency coverage it is difficult to discern the exact physical mechanisms responsible for such a suppression. Finally, Bait et al. (2024) in a recent radio follow-up study of a sub-sample of LzLCS sources found that the $f_{\text{esc}}^{\text{LyC}}$ (and the O_{32} , SFR density) depends on the radio spectral index (specifically measured between 3–6 GHz). These results motivate a detailed radio-SED study of LCEs to better understand the physical processes governing these relations.

Here, we present new multi-frequency radio-SED observations of a sample of eight xSFGs selected from Izotov et al. (2020, 2024) and Jaskot et al. (2019). Our multi-frequency RC observations were conducted using the NRAO¹ Karl G. Jansky Very Large Array (VLA) at 6 (C-band), 3 (S-band), and (a sub-sample) at 1.5 (L-band) GHz. We also combine new observations with the upgraded Giant Metrewave Radio Telescope (uGMRT) at Band-5 (1060 - 1460 MHz) together with archival LOW Frequency ARray (LOFAR) data at 120-168 MHz data using the LOFAR Two-metre Sky Survey Data-Release 2 (LoTSS DR2; Shimwell et al. 2017, 2022).

¹ The National Radio Astronomy Observatory is a facility of the National Science Foundation operated under cooperative agreement by Associated Universities, Inc.

Our paper is organized as follows. In Section 2 we describe our sample, VLA and uGMRT observation setup, data analysis and RC flux density measurements in different radio bands. In Section 3 we first present the observed radio-SED of our sample and the various model radio-SEDs that represent our sample. We then present the dust attenuation measurement using our radio observations. In Section 4, we discuss, 1) the cause(s) of the lack of non-thermal emission in xSFGs based on our well-sampled radio-SED, 2) the relationship between $f_{\text{esc}}^{\text{LyC}}$, O_{32} , metallicity, and radio spectral index for xSFGs and 3) the overall implications of our observed radio-SED to better understand the extreme nature of high- z galaxies found using the JWST. We then summarize our main results and conclude in Section 5.

2. Data

In this section, we describe our sample selection and new VLA observations at multiple observing bands, namely: the S (2 - 4 GHz), C (4 - 8 GHz), X (8 - 12 GHz) and Ku (12-18 GHz) bands. We support these observations with new low frequency data using the uGMRT at Band-5 (1060 - 1460 MHz). We also present archival LOFAR data (120 - 168 MHz) covering most of our sample. We also describe our calibration and imaging strategy.

2.1. Sample

Our sample is selected from the recently identified sample of xSFGs at low- z , $z \sim 0.01-0.06$, from Izotov et al. (2020, 2024) and Jaskot et al. (2019) (see also Yang et al. 2017). All our sources have extremely low-metallicity ($12+\log \text{O}/\text{H} \sim 6.98-7.88$), low stellar mass ($\log (M_*/M_\odot) \sim 5.8 - 8.6$), very high $\text{O}_{32} (\geq 15$ to up to ~ 53) and high $\text{H}\beta$ equivalent width ($\text{EW}(\text{H}\beta) \geq 250 \text{ \AA}$). We observed several of these sources at S- and C-bands using the VLA with the B-configuration (PI: Bait; Project Code: 23A-138 & 24A-103) and at higher frequency bands at X- and Ku with the C-configuration (PI: Bait; Project Code: 24A-103). We also conducted follow-up uGMRT Band-5 observations (PI: Bait, Proposal ID: 43_062 and 45_075) for our sample of xSFGs.

Here we aim to study the radio-SED primarily at GHz frequencies. We thus present a sample of 8 xSFGs which has a seamless RC coverage between $\sim 1 - 12$ GHz (S- to X-band) from the two VLA and uGMRT programs. Except for one source (J0159+0751), all our sources also have Ku-band (12 - 18 GHz) observations (Project Code: 24A-103). For two sources, J150934+373146 and J160810+352809, we use the published Band-5 data from Sebastian & Bait (2019) (SB19 hereafter). J1032+4919 was also observed with the VLA at L-band (1 - 2 GHz; under Project Code: 23A-138). We also present LOFAR 150 MHz data which covers 7 out of the 8 sources from our sample. The various physical properties (e.g., metallicity, O_{32} , V_{sep} , observed and dust extinction corrected $\text{H}\beta$ line flux) of the 8 xSFGs studied here are taken from Izotov et al. (2020, 2024) and Jaskot et al. (2019) and shown in Table 1.

In the next section, we present details on the new RC observations at multiple VLA and uGMRT bands together with archival LOFAR observations. Table 2 provides a brief summary of these observations.

2.2. VLA L-, S-, C-, X- and Ku-band Observations and Data Analysis

We used the default VLA setup for our L-, S-, and C-band continuum observations. For the L- and S-bands we used a total

bandwidth of 1 and 2 GHz respectively with a 8-bit sampler. The L-band (S-band) was split into one (two) baseband(s) each comprising of 8×128 MHz subbands. For the C-band we used a total bandwidth of 4 GHz with a 3-bit sampler which was split into two basebands each comprising of 16×128 MHz subbands. For each of these cases, the subbands were further split into 64 channels. All of these observations were performed in the B-configuration. This setup is identical to the previously followed setup for RC observations of the LzLCS sources at L-, S- and C-bands from Bait et al. (2024). We adopted the standard observing strategy used for continuum observations at L-, S- and C-bands which was also followed for the LzLCS sources (see Bait et al. 2024, for details). Briefly, after an initial setup, we observed the flux density scale calibrator (for 3 - 5 mins). We then alternative between the phase calibrator (~ 1 min per cycle) and the target ($\sim 5 - 6$ mins per cycle). The S- and C-band observations were conducted within a single scheduling block (SB) lasting approximately ~ 1 hr. We achieved an on-source integration time of 22 mins each for S- and C-band. For the L-band SBs typically lasted for a duration of ~ 1 hr and 40 mins, where we achieved an on-source integration time of ~ 75 mins.

For the high-frequency X- and Ku-band observations we again used the default VLA setup, with a total bandwidth of 4 GHz and 6 GHz respectively with a 3-bit sampler. The total bandwidth for the X-band (Ku-band) was split in 2 (3) subbands each comprising 16×128 MHz subbands. Here as well each subband was further split into 64 channels. These observations were performed in the C-configuration. After an initial setup, we observed the flux density scale calibrator for approximately 5 mins. For the Ku-band an additional scan of ~ 4 mins for pointing calibration was performed, where the phase calibrator was used as a pointing calibrator. We then alternative between the phase calibrator (~ 2 mins per cycle) and the target (~ 8 mins per cycle). We achieved an on-source integration time of ~ 15 mins for both the X- and Ku-band.

For all our VLA data reduction, we used the Common Astronomy Software Applications (CASA) data processing software (McMullin et al. 2007; THE CASA TEAM et al. 2022). We followed a similar data reduction procedure as described in Bait et al. (2024). Briefly, each SB was initially flagged and calibrated using the standard VLA calibration pipeline v6.5.4. We manually inspected the calibrated flux density scale and phase calibrators for each SB. Any leftover RFI and poorly performing antennas were manually flagged. And the VLA pipeline was then re-run.

We then extracted the calibrated target and inspected for any leftover RFI in some spectral windows, which was then further flagged. Then we proceeded with the imaging of these data using CASA `TCLEAN`. For S- and C-bands, since these were observed in the multi-band mode, we first split the target in S- and C-band before imaging (see Bait et al. 2024). For all our imaging, CASA `TCLEAN` was setup to use the multi-term multi-frequency synthesis (mtmfs) algorithm (Rau & Cornwell 2011) where the `NTERMS` were set to 2 and a `ROBUST` value of 0.5 was used. The flux density and corresponding error (σ) was then estimated by manually making elliptical regions around each of the target sources using CASA task `IMVIEW`, and a 2D Gaussian fit was performed using the task `IMFIT` (see Bait et al. 2024, for more details on this procedure). For one marginally resolved source in our sample, J150934+373146 which is also relatively extended in the optical compared to other xSFGs, the flux density and error was measured using PyBDSF (the Python Blob Detector and Source Finder; Mohan & Rafferty 2015). Table 3 presents the flux density, noise (σ). For non-detections, where sources have a signal-

Table 1: Basic properties of our sample of xSFGs.

Target	RA (deg)	DEC (deg)	z	$12 + \log \text{O}/\text{H}$	$\log M_*/M_\odot$	O_{32}^a	SFR^b (M_\odot/yr)	Lit. source
J0159+0751	29.96979	+7.86356	0.06105	7.56	8.6	39.0	2.3	Izotov et al. (2020)
J0811+4730	122.96721	+47.50729	0.0444	6.98	5.88	5.9	0.19	Izotov et al. (2024)
J0820+5431	125.08029	+54.52781	0.03851	7.49	6.0	22.0	0.2	Izotov et al. (2020)
J1032+4919	158.23633	+49.32979	0.0442	7.59	6.8	24.0	2.4	Izotov et al. (2020)
J1355+4651	208.85692	+46.86426	0.02811	7.56	5.8	23.0	0.1	Izotov et al. (2020)
J150934+373146	227.39239	+37.52948	0.0325	7.88	8.1	15.1	1.35	Jaskot et al. (2019)
J160810+352809	242.04318	+35.46926	0.0327	7.83	7.5	34.9	0.46	Jaskot et al. (2019)
J2229+2725	337.38829	+27.42378	0.07622	7.08	6.96	53.0	0.68	Izotov et al. (2024)

Notes. The physical properties presented here are taken from the literature values shown in the last column.

^a $\text{O}_{32} \equiv [\text{OIII}] \lambda 5007 / [\text{OII}] \lambda 3727$.

^b The SFR is derived using the dust-corrected $\text{H}\beta$ line using the relation from Kennicutt (1998). For J150934+373146 and J160810+352809 the $\text{H}\alpha$ line was used and the relation from Kennicutt & Evans (2012). See the references (last column) for details.

to-noise ratio (S/N) below 3, we present the 3σ upper limits as the flux density. Table 3 also shows the synthesized beam properties (beam major/minor axis and position-angle) from our observations in various bands. Note that for all further analysis on the RC flux density, spectral index and radio-SED analysis we add a 5% calibration error in quadrature (following Bait et al. 2024).

2.3. uGMRT Band-5 Observations and Data Analysis

For the uGMRT Band-5 (1460 - 1060 MHz) observations, we used a total bandwidth of 400 MHz split in 2048 channels, similar to that used in SB19.

The data reduction was carried out using the YARP² package. YARP comprises a collection of high-level Python recipes to perform flagging, calibration and imaging which are based on various standard CASA tasks at the lowest-level. The different flagging, calibration and imaging recipes can be combined to design custom radio data reduction pipelines/workflows for both continuum and spectral line data. The YARP package was first used for GMRT Hr 21-cm spectral-line data reduction in Paudel et al. (2023), and a detailed paper describing the package is in preparation.

Here we use the YARP package with CASA v6.5.5 to design a custom pipeline for our uGMRT Band-5 continuum data reduction. Briefly, in this pipeline the raw uGMRT data initially underwent a round of flagging using the CASA task `TCROP`. Here any bad/non-working antennas were also flagged which was manually provided to YARP. This data then underwent 5 rounds of calibration (flux, phase and bandpass) and flagging (which used a combination of CASA tasks `TCROP`, `RFLAG` and `CLIP`). The calibrated data for phase calibrator, flux density scale calibrator and target was manually inspected for any leftover RFI. We then extracted the calibrated target and self-calibrated the data. Each self-calibration round includes three rounds of phase-only self-calibration and one round of Amplitude and Phase self-calibration. For a few cases, the residual (data - model) was flagged using CASA task `RFLAG` and the flags were applied to the data before proceeding to another round of self-calibration. This final calibrated data was then used for imaging using the `MTMFS` algorithm with `NTERMS` set to 2. For all our new Band-5 observa-

tions presented here, we do not detect any emission and thus we present the 3σ upper limits. For two xSFGs, J150934+373146 and J160810+352809, the flux density and noise are taken from SB19. Note that J1032+4919 was also observed by SB19 and was also not detected. Our upper limits for J1032+4919 are consistent with SB19. Table 3 presents the flux properties for our sample.

2.4. Archival LoTSS DR2 data

We also present archival LoTSS (120-168 MHz) DR2 imaging data (Shimwell et al. 2022) for our sample. We download cutouts around each of the sources in our sample using the LoTSS DR2 cutout service³. We inspected each image to search for detections. Out of the 7 sources which have LoTSS coverage, we detected emission in only one source, J150934+373146. The flux was estimated using PyBDSF. For the rest of the sources we present the 3σ upper limits (see Table 3).

Table 2: Brief summary of the new multi-frequency radio observations.

Tel.	Band	Cen. Freq. ^a (GHz)	BW ^b (GHz)	TOS ^c (mins)	Array ^d
uGMRT	Band-5	1.25	0.4	120	Full
VLA	L	1.5	1	75	B
VLA	S ^e	3.0	2	20	B
VLA	C ^e	6.0	4	20	B
VLA	X	10.0	4	15	C
VLA	Ku	15.0	6	15	C

Notes. ^a Central frequency of the observing band.

^b Total Bandwidth.

^c Time on source (approximate values).

^d VLA configuration.

^e The S- and C-band observations were performed simultaneously in a multi-band mode.

² The current development version of the YARP package can be found here: <https://github.com/omkarbait/yarp/>

³ https://lofar-surveys.org/dr2_release.html

Table 3: Radio Fluxes of xSFG.

Freq. (GHz)	Details ^a	J0159+0751	J0811+4730	J0820+5431	J1032+4919	J1355+4651	J150934+373146	J160810+352809	J2229+2725
1.25	S_ν (μ Jy)	< 64.5	< 58.2	< 69.3	< 48.3	< 46.2	478 ± 36.9^b	58 ± 17.0^b	< 79.8
	$\theta_{\text{maj}} \times \theta_{\text{min}}$ P.A.	$2.3'' \times 2.1''$ 56.2°	$2.4'' \times 1.9''$ 21.1°	$5.0'' \times 2.3''$ 85.4°	$2.4'' \times 2.2''$ 7.4°	$4.0'' \times 2.1''$ -35.6°	$3.1'' \times 2.6''$ -69.7°	$7.3'' \times 3.3''$ 55.4°	$3.9'' \times 2.0''$ 44.0°
1.5	S_ν (μ Jy)	--	--	--	< 41.1	--	--	--	--
	$\theta_{\text{maj}} \times \theta_{\text{min}}$ P.A.	--	--	--	$3.8'' \times 3.5''$ -40.8°	--	--	--	--
3.0	S_ν (μ Jy)	< 36.6	< 27.3	< 31.8	68.7 ± 9.6	< 32.7	330.0 ± 39.6	-- ^c	< 29.7
	$\theta_{\text{maj}} \times \theta_{\text{min}}$ P.A.	$3.3'' \times 1.8''$ 55.4°	$2.7'' \times 1.9''$ 68.5°	$2.0'' \times 1.7''$ 38.6°	$2.3'' \times 1.8''$ -83.8°	$1.9'' \times 1.7''$ 49.7°	$6.5'' \times 1.7''$ 59.9°	$2.4'' \times 1.8''$ 84.3°	$2.3'' \times 1.8''$ 71.1°
6.0	S_ν (μ Jy)	34.6 ± 6.4	< 16.8	< 18.9	61.9 ± 5.7	< 19.8	170.0 ± 15.14	46.45 ± 4.6	< 18.6
	$\theta_{\text{maj}} \times \theta_{\text{min}}$ P.A.	$1.6'' \times 1.0''$ 50.0°	$1.5'' \times 1.0''$ 66.0°	$1.2'' \times 0.9''$ 42.4°	$1.2'' \times 1.0''$ -62.0°	$1.1'' \times 0.9''$ 43.5°	$2.4'' \times 1.0''$ 63.6°	$1.1'' \times 1.0''$ 89.7°	$1.1'' \times 1.1''$ 57.6°
10.0	S_ν (μ Jy)	36.0 ± 6.6	< 18.4	< 39.9	53.9 ± 6.8	31.0 ± 6.6	210.0 ± 12.16	43.5 ± 7.6	< 16.7
	$\theta_{\text{maj}} \times \theta_{\text{min}}$ P.A.	$4.4'' \times 1.9''$ -56.0°	$3.4'' \times 1.9''$ 79.4°	$2.8'' \times 1.9''$ -83.4°	$3.9'' \times 1.8''$ -74.6°	$5.5'' \times 1.8''$ 64.3°	$2.0'' \times 1.9''$ 41.7°	$2.1'' \times 1.8''$ -19.3°	$2.7'' \times 1.9''$ -75.8°
15.0	S_ν (μ Jy)	--	< 17.2	--	69.0 ± 5.0	28.3 ± 5.4	180.0 ± 22.42	45.14 ± 6.0	< 13.9
	$\theta_{\text{maj}} \times \theta_{\text{min}}$ P.A.	--	$1.6'' \times 1.3''$ -70.7°	--	$1.4'' \times 1.2''$ 7.4°	$2.0'' \times 1.2''$ 89.7°	$3.1'' \times 1.3''$ 73.1°	$2.5'' \times 1.3''$ 71.6°	$2.9'' \times 1.3''$ 67.0°
0.150	S_ν (μ Jy)	--	< 532.4	< 169.5	< 200.2	< 181.9	400.68 ± 126.6	< 225.8	< 316.0
	$\theta_{\text{maj}} \times \theta_{\text{min}}$ P.A.	--	$6'' \times 6''$ 90°	$6'' \times 6''$ 90°	$6'' \times 6''$ 90°	$6'' \times 6''$ 90°	$6'' \times 6''$ 90°	$6'' \times 6''$ 90°	$6'' \times 6''$ 90°

Notes. Sources with no observations in a specific band are shown with empty values.

^a Shows the measured flux density (S_ν) and beam parameters for each observing frequency. For non-detections we present the 3σ upper limits on the flux densities.

^b Flux densities and beam parameters taken from SB19.

^c The VLA S-band flux density for this source could not be measured due to strong artefacts from a neighbouring bright source.

3. Results

We present the radio-SEDs of our sample of xSFGs spanning a wide range of radio frequencies from 1.2 GHz (from 150 MHz for J150934+373146) to up to 15 GHz using a combination of VLA, uGMRT, and LOFAR telescopes described in Section 3.1.

3.1. Radio-SEDs of xSFGs

As seen from Figure 1, most sources (except J1355+4651) can be described as being flat between 6-15 GHz, with several sources showing evidence for a strong turnover at lower frequencies. The turnover frequency (ν_t) lies in the range of 2 – 5 GHz. J1355+4651 has a flat spectrum between 10 – 15 GHz and shows a turnover close to 10 GHz. Besides that at lower frequencies (< 6 GHz) there is a diversity in the radio-SED. For J0159+0751, the 3σ upper limit at 3.0 GHz from the VLA S-band data suggests either a flat spectrum or possibly a turnover. Two other sources, J150934+373146 and J160810+352809, are exceptions to this general feature in the radio-SED. J160810+352809 has a flat radio spectrum down to 1.2 GHz, with no significant evidence for a turnover in our current data. The radio-SED of J150934+373146, on the other hand, has the most complex features in our sample. The spectrum is relatively flat (within the error bars) between 6-15 GHz, and is fairly steep ($\alpha \approx -1.0$) below 6 GHz to up ~ 1 GHz. Between 1 GHz - 150 MHz range it shows evidence for a turnover (or flattening).

The presence of a strong turnover at lower frequencies in the radio spectrum of star-forming galaxies can be a signature of free-free absorption (FFA)⁴. The radio spectrum can show such a turnover at GHz frequencies due to a high emission measure (EM), owing to high ionised gas density (H04). SBS 0335-052, a nearby low-metallicity starburst, also shows such a turnover but at a slightly lower frequency of ~ 1.5 GHz, although at higher frequencies it is relatively steeper than xSFGs in our sample (H04).

We particularly, consider two radio-SED models,

- Simple Model: Here the total radio emission (S_ν) comprises of a mix of a single thermal (S_ν^{th}) and non-thermal component (S_ν^{nth}), described as:

$$S_\nu = S_\nu^{\text{th}} + S_\nu^{\text{nth}} = A_1 \left(\frac{\nu}{\nu_o} \right)^{-0.1} + A_2 \left(\frac{\nu}{\nu_o} \right)^{\alpha_{\text{nth}}}. \quad (1)$$

Here, ν is the observed frequency, ν_o is a reference frequency which is fixed to 1 GHz in all our models. And the α_{nth} is the non-thermal spectral index, which we fix to a canonical value of -0.8 (Condon 1992; Bait et al. 2024). We then define the thermal fraction at a reference frequency of 1 GHz ($f_{1\text{GHz}}^{\text{th}}$) as

$$f_{1\text{GHz}}^{\text{th}} = S_{1\text{GHz}}^{\text{th}} / S_{1\text{GHz}}.$$

- FFA Model: Here the radio-SED shows a strong turnover at lower frequencies due to the effect of FFA arising due to high EM in the ISM. We define the turnover frequency (ν_t) as the frequency at which the free-free absorption optical depth (τ_ν^{ff}) becomes 1 (see e.g., Hunt et al. 2004; Clemens et al. 2010; Galvin et al. 2018). The EM is thus directly related

to ν_t , such that increasing the EM leads to a higher value of ν_t . Specifically, in this work we used the relation from H04 (their Eq. 1) to derive the EM. We model the effect of FFA assuming that the absorbing medium is intermixed with both the thermal and the non-thermal components, following (H04, Model 2);

$$S_\nu = \frac{1 - \exp(-\tau_\nu^{\text{ff}})}{\tau_\nu^{\text{ff}}} (S_\nu^{\text{th}} + S_\nu^{\text{nth}}). \quad (2)$$

In this model the free parameters are: a) EM, b) θ (angular size of the emitting region) and c) $S_{\nu_o}^{\text{nth}}$. We also derive the $f_{1\text{GHz}}^{\text{th}}$ for the FFA model following the above definition. In general, H04 introduces two other FFA models depending on the geometry of the absorbing medium. These are the foreground screen absorption model (Model 1) and an absorption screen affecting only the non-thermal component (Model 3). Given our limited number of data points in which we have a detection, it is difficult to perform a formal fit across these models to rule them out and/or to perform a parameter fitting.

Next we describe the individual sources which are best described by one of the above radio-SED models. Note that we did not perform a formal fit to the parameters, since given our limited number of data points with detections, we cannot remove the several degeneracies in the parameters. Importantly, to constrain ν_t in the FFA model, we need detections below the turnover, however, currently, we only have upper limits. We thus present the radio-SED models with indicative parameters which can overall describe the observed radio-SED, wherein there could be some degeneracy between these parameters.

- J160810+352809: This source has a flat radio spectrum from 1.2 - 15 GHz, and can thus be easily modelled with a ‘‘Simple Model’’ with a higher thermal fraction ($f_{1\text{GHz}}^{\text{th}} \sim 0.98$) as shown by the grey line in Figure. 1. However, given the relatively larger error bar at 1.2 GHz, we cannot completely rule out FFA at low frequencies.
- J0159+0751, J1032+4919, J1355+4651: These sources have flat spectra at high frequency and the upper limits at low-frequencies suggest a turnover in the spectra due to FFA. In Figure 1 we overplot the grey lines which show the ‘‘FFA model’’ with a high $f_{1\text{GHz}}^{\text{th}} \sim 0.46 - 0.77$, a ν_t in the range of $\sim 2 - 10$ GHz and a typical size of this emitting region in the $\sim 1''$ range. For J0159+0751 the 3σ upper limit at 3 GHz is in principle also consistent with a thermally dominant spectrum with no FFA ($f_{1\text{GHz}}^{\text{th}} \approx 1$; shown with a green line) similar to J160810+352809. For J1355+4651 since the ν_t is close to 10 GHz, we only have two detections at 10 and 15 GHz. It is possible that there is a larger fraction of non-thermal emission at lower frequencies, which is absorbed due to FFA. Thus, the true $f_{1\text{GHz}}^{\text{th}}$ for this source can be lower than what we have presented. This source has the highest ν_t in our sample and here even with detections at low frequencies, it will be very difficult to constrain $f_{1\text{GHz}}^{\text{th}}$. The EM in these sources is very high, in the range of $\sim (4 - 80) \times 10^7$ pc cm⁻⁶ (see Table 4). SBS 0335-052 also has a EM of $\sim (2 - 8) \times 10^7$ pc cm⁻⁶ which is within this range. This value of EM is $\sim 1 - 3$ orders of magnitude higher than that found in typical nearby star-forming galaxies (e.g., Chyży et al. 2018; Grundy et al. 2024).
- J150934+373146: Lastly J150934+373146 has the most complex radio-SED in our sample. Here the radio-SED below 10 GHz is consistent with a steep spectrum and a turnover at a relatively lower value of 0.41 GHz (EM

⁴ Synchrotron self-absorption (SSA) can also lead to low-frequency turnovers. However, the brightness temperature (T_b) of our sources is too small (≤ 100 K) for SSA to be significant at GHz frequency range, which will require an extremely high $T_b \approx 10^{12}$ K (Condon & Ransom 2016).

⁵ In the following, we use this sign convention to define the spectral index. Note that some references use the opposite sign convention.

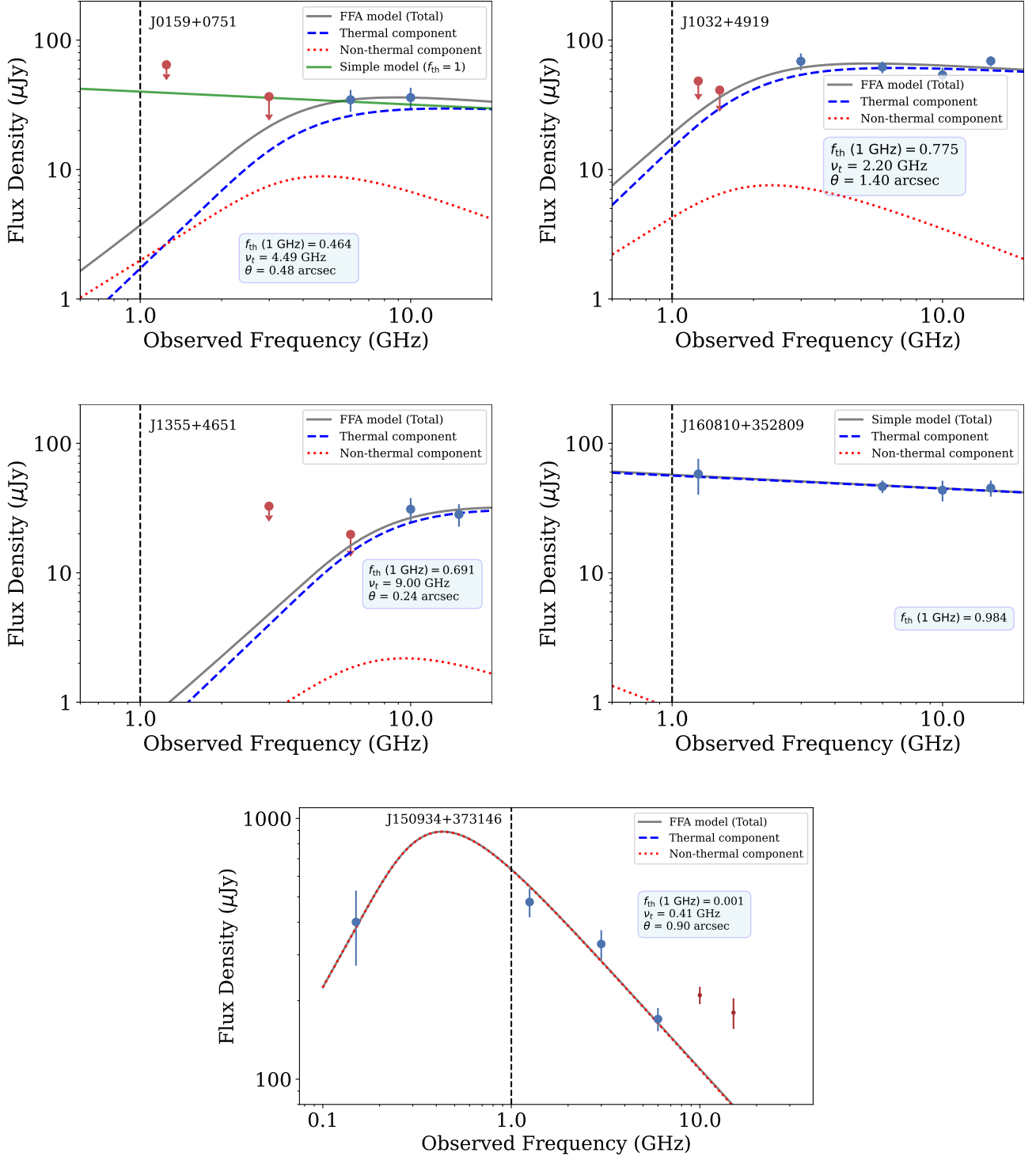


Fig. 1: Observed radio-SEDs of xSFGs for our detection sample. RC detections are shown in blue error bars (with 1σ errors), and non-detections (3σ upper limits) are shown in red arrows. We overlay the radio-SED with different models (FFA and simple) in solid grey line. We also show the thermal (blue dashed line) and non-thermal (red dotted line) component of the radio-SED model for each of our sources. Note that the radio-SED model parameters are “indicative” values and are not derived using a formal fit. J0159+0751 is also compatible with a purely thermal model (simple model with $f_{\text{th}}^{\text{1GHz}} = 1$) shown in green line. For J150934+373146 we show the FFA model (dashed line) which explains the low-frequency data points (< 10 GHz). At high-frequencies (shown in brown) there appears to be break from a single FFA model. Note that here the thermal component of the radio-SED model is not visible in the plot as the source is possibly strongly non-thermally dominant. See Sec. 3.1 for a discussion on radio-SED models.

$1.2 \times 10^6 \text{ pc cm}^{-6}$). The radio-SED is possibly non-thermally

dominant as opposed to the rest of the sample. Peculiarly, the

radio-SED at high frequencies (> 10 GHz) shows a break from the steeply spectrum and rather shows a rising spectrum. Thus it is apparent that the radio-SED cannot be modelled by a simple or FFA model. This could require a combination of two FFA components, having two different ν_i , a high value close to 10 GHz and a lower value of 0.4 GHz (see also Section 4 for a discussion).

In Table 4 we show the various physical properties with parameters (indicative values) derived from the above described radio-SED models.

3.2. Comparison between $H\beta$ dust attenuation derived using Balmer lines and RC emission

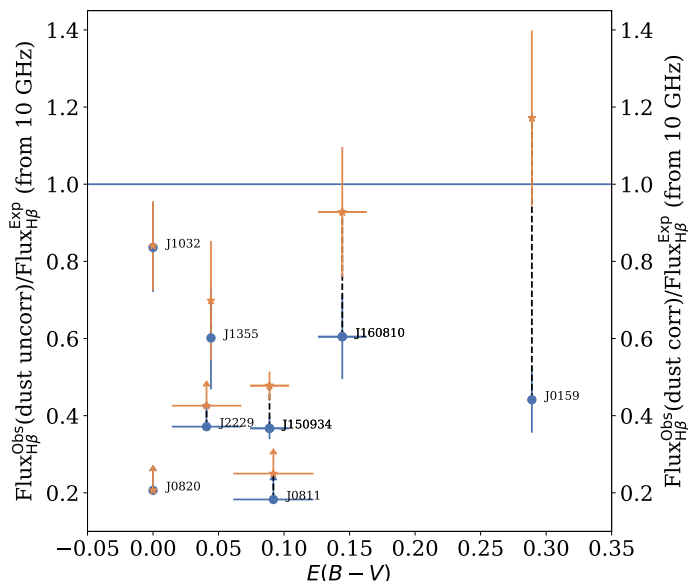


Fig. 2: Left-axis: Ratio of the observed $H\beta$ flux density (dust uncorrected) to that expected from the 10 GHz flux density vs. $E(B-V)$. Right-axis: Same as left axis except that the observed $H\beta$ flux density is corrected for dust. The dashed line connects the points with and without dust correction. Overall we find that in spite of correcting the $H\beta$ flux density for dust extinction using hydrogen Balmer decrement, in a few cases (e.g., J1032+4919 and J1355+4651) it is possible that a small fraction ($\sim 20 - 30\%$) of the ionizing radiation emitted by the galaxy is not visible in the Balmer lines. See Sec. 3.2 for a detailed discussion and caveats.

Based on the radio-SEDs presented above, we can see that the RC emission at high frequencies (≥ 10 GHz) for most of our sample is dominated by the free-free component. Importantly, RC emission at this frequency is not affected by dust extinction. Since the free-free emission in a galaxy at both the radio and optical wavelengths arise from the same emitting regions, we can use the RC flux density at 10 GHz to independently derive the expected dust-free $H\beta$ flux density ($\text{Flux}_{H\beta}^{\text{Exp}}$). In Appendix A, we describe the details on measuring $\text{Flux}_{H\beta}^{\text{Exp}}$ using RC emission at 10 GHz. Table 4 shows the derived $\text{Flux}_{H\beta}^{\text{Exp}}$ for our sample. We can then use the ratio between the observed $H\beta$ (uncorrected for dust) and $\text{Flux}_{H\beta}^{\text{Exp}}$ to measure the total dust-extinction. We use the observed and dust-extinction corrected $H\beta$ flux densities from Izotov et al. (2020) and Izotov

et al. (2024) which are derived from the SDSS spectrum. For J150934+373146 and J160810+352809, we measured the $H\beta$ line flux density from their SDSS spectrum. We estimated the dust extinction at $H\beta$ ($A_{H\beta}$) following the procedure described in Izotov et al. (2016b)⁶, where we use the V-band extinction (A_V) from Jaskot et al. (2019) and assume a R_V of 2.7 (Izotov et al. 2017a).

In Figure 2 (left-axis), we compare this ratio against $E(B-V)$ ⁷. In the right-axis of Figure 2, we compare the ratio between the dust-corrected $H\beta$ flux density, derived using hydrogen Balmer decrement, and $\text{Flux}_{H\beta}^{\text{Exp}}$ with $E(B-V)$. Using such a ratio we can compare if the dust correction applied to the observed $H\beta$ line is completely accounted for by the Balmer decrement. For the cases when this ratio is below 1, we can interpret this as evidence of a fraction of ionizing radiation emitted by the galaxy being missed in the Balmer lines. Note that for a few sources the uncertainties of $E(B-V)$ are too small and are not apparent on the figure.

From Figure 2 (left-axis), we find that many sources in our sample show evidence of dust attenuation at optical wavelengths. It is intriguing to find the presence of dust in such low-mass and low-metallicity systems. We notice that despite the dust-correction from the Balmer decrement to the $H\beta$ line, it is possible that some ionizing radiation emitted by the galaxy is missing from the Balmer lines (e.g., in J1032+4914 and J1355+4651). In the case of J1032+4914 and J1355+4651, which have $E(B-V)$ values close to zero and thus also have a negligible dust correction to the $H\beta$ line, yet they show evidence for such a missing emission using the radio-derived $\text{Flux}_{H\beta}^{\text{Exp}}$. The amount of ionizing emission missed in these objects is generally small, between $\sim 20 - 30\%$. However in J1355+4651, as described in Section 3.1, it is possible that there is a higher amount of non-thermal emission which is difficult to account for due to non-detections below 10 GHz. This can reduce the $\text{Flux}_{H\beta}^{\text{Exp}}$ thus making it compatible with the dust-corrected $H\beta$ line flux. In some cases, for example, in J150934+373146, J0820 + 5431 and J0811 + 4730, there is apparently a large fraction of ionizing emission missing from the Balmer lines. As shown in Section 3.1, J150934+373146 has a large fraction of non-thermal emission and thus the true $\text{Flux}_{H\beta}^{\text{Exp}}$ is lower than our estimated value. Moreover, J150934+373146 has an extended structure, thus we could be missing some $H\beta$ flux from the SDSS spectrum. Both these effects could reduce the fraction of missing ionizing emission in the Balmer lines than our estimate. In J0820+5431 and J0811+4730 due to non-detections in the RC emission, we can only present a lower limit on the total dust extinction in the $H\beta$ line. J0159+0751 has the highest $E(B-V)$ value in our sample and the ratio between the observed $H\beta$ and $\text{Flux}_{H\beta}^{\text{Exp}}$ flux is also relatively low. Contrary to other sources, both J0159+0751 and J160810+352809 have $\text{Flux}_{H\beta}^{\text{Exp}}$ consistent with that derived using the dust-corrected $H\beta$ line within the uncertainties (see Figure 2).

Overall, we observe a large variation in the dust properties of xSFGs with evidence for a small fraction of the ionizing radiation emitted by the galaxy missed in the Balmer lines.

⁶ Here the $A_{H\beta}$ is derived using $C(H\beta)$ which depends on the A_V and R_V . Effectively this assumes the Cardelli et al. (1989) extinction law which is found to be a better fit for such extreme galaxies (Izotov et al. 2017a).

⁷ Here $E(B-V)$ is derived using the $C(H\beta)$ values from Izotov et al. (2020) and Izotov et al. (2024), and using $C(H\beta) = 1.47 \times E(B-V)$.

Table 4: Physical properties of xSFGs from our RC observations.

Target	$f_{1\text{GHz}}^{\text{th } a}$	EM^b	N_e^c	$\text{Flux}_{\text{H}\beta}^{\text{Exp } d}$	$\alpha_{\text{high}}^{\text{low } e}$	$f_{\text{esc}}^{\text{LyC}} \text{ (indirect)}^f$	radio-SED Model
J0159+0751	0.464	18.85	660 ± 300	84.76 ± 16.26	$0.078_{\text{X}}^{\text{C}} \pm 0.021$	0.091 ± 0.03	FFA/Simple ($f_{1\text{GHz}}^{\text{th}} \approx 1$)
J1032+4919	0.775	3.95	560 ± 50	130.39 ± 17.85	$-0.150_{\text{C}}^{\text{S}} \pm 0.027$	---	FFA
J1355+4651	0.691	80.26	1200 ± 150	73.33 ± 16.15	$-0.222_{\text{Ku}}^{\text{X}} \pm 0.065$	0.169 ± 0.03	FFA
J150934+373146	0.001	0.12		501.44 ± 38.36	$-0.958_{\text{C}}^{\text{S}} \pm 0.158$	0.034 ± 0.01	FFA ^g
J160810+352809	0.984	---		103.87 ± 18.88	$-0.128_{\text{X}}^{\text{C}} \pm 0.027$	0.31 ± 0.13	Simple

Notes. The various parameters from the radio-SED models presented here are indicative values which can overall describe the observed radio-SED and are not derived using a formal fit with a full analysis of parameter degeneracy.

^a The thermal fraction is defined at 1 GHz for reference and is derived from the radio-SED models shown in Fig. 1, and it not fitted with the data at ~ 1 GHz.

^b In units of $10^7 \times \text{pc cm}^{-6}$. Here we use the T_e values from Izotov et al. (2020) and Izotov et al. (2024). For J150934+373146 and J160810+352809 we use a fixed value of $2 \times 10^4 \text{K}$.

^c In units of cm^{-3} . Values are taken from Izotov et al. (2020, 2024).

^d Values shown are in units of $10^{-16} \text{ ergs/s/cm}^2$. Derived using the 10 GHz flux density. See Appendix A for details.

^e The VLA bands used to derive $\alpha_{\text{high}}^{\text{low}}$ is shown around each value.

^f $f_{\text{esc}}^{\text{LyC}}$ values taken from Izotov et al. (2020, 2024) which are indirectly estimated using V_{sep} (Izotov et al. 2018b). For J150934+373146 and J160810+352809 the $f_{\text{esc}}^{\text{LyC}}$ are derived here using V_{sep} from Jaskot et al. (2019).

^g The radio-SED shows a deviation from a single FFA model at high-frequencies.

4. Discussion

4.1. RC suppression in xSFGs at low frequencies

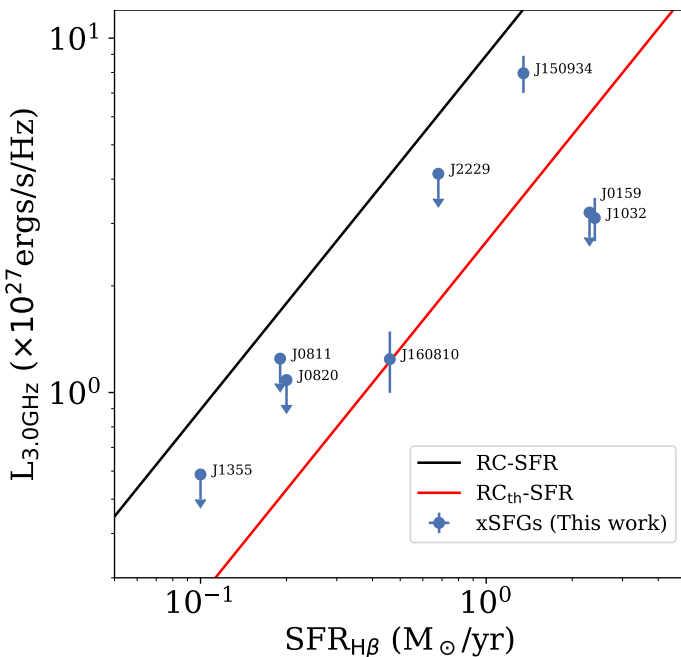


Fig. 3: xSFGs on the RC-SFR relation at 3 GHz. We show the standard total RC-SFR relation (Murphy et al. 2011) using a $\alpha_{\text{nth}} = -0.8$ with a solid black line. We also show the RC_{th} -SFR relation with a red solid line. In both these cases we have used a fixed value of $T_e = 20000 \text{K}$. Our xSFGs show a significant suppression of RC emission than that expected from the total RC-SFR relation. See Section 4.1 for a discussion.

In Figure 3, we plot the observed RC luminosity at 3 GHz against the SFRs for our sample of xSFGs. Our SFRs are taken from the literature (see Table 1) and are derived using the dust-corrected $\text{H}\beta$ and $\text{H}\alpha$ line luminosity following the (Kennicutt 1998; Kennicutt & Evans 2012) relation. For reference, we overplot the RC (total)-SFR relation at 3 GHz for star-forming galaxies from Murphy et al. (2011, Eq. 15) assuming a α_{nth} of -0.8 , shown in solid black line. The thermal RC (RC_{th}) - SFR relation from Murphy et al. (2011, Eq. 11) is shown in solid red line. Note that for J160810+352809, since we were unable to measure the flux density at 3 GHz (see Table 3), we have used the modelled RC flux density at 3 GHz from Section 3.1 and a noise level of $10 \mu\text{Jy}$ typically achieved at S-band for our observations. We note that all our xSFGs show suppressed RC emission than that expected from the RC-SFR relation at 3 GHz, with a few sources even below the RC_{th} - SFR relation. We notice a similar trend in our data at 1.25 GHz using the uGMRT data.

Previous single band radio studies of xSFGs at low-frequencies (150 MHz and ~ 1.5 GHz) had also found that the RC emission in such galaxies is suppressed (Chakraborti et al. 2012; Sebastian & Bait 2019; Borkar et al. 2024), which was indirectly associated with a lack of non-thermal emission. Our finding of a thermally dominant radio-SED of xSFGs provides conclusive evidence for the prevalence of such a scenario. Moreover the effect of FFA at GHz frequencies could further suppress the RC emission. For example, the RC emission in J1032+4919 was found by SB19 to be highly suppressed at 1.2 GHz compared to other sources in their sample and was the only undetected source in their study. Our radio-SED observation suggests that this non-detection is due to FFA at ~ 2.2 GHz. In some systems RC emission can get suppressed due to FFA even in the presence of non-thermal emission (e.g., in J150934+373146).

In general, there are several scenarios which can lead to a lack of non-thermal emission: 1) extremely young ages (< 5

Myrs) which lack enough SNe (e.g., Hayes et al. 2007; Carilli et al. 2008; Chakraborti et al. 2012; Greis et al. 2017; Sebastian & Bait 2019), 2) CR escape (Lisenfeld et al. 2004; Sebastian & Bait 2019), 3) strong synchrotron losses due to enhanced magnetic fields (Chakraborti et al. 2012) and 4) Inverse Compton (IC) losses due to high photon density (Condon 1992). The young ages of these galaxies are probably the primary reason for the flat spectrum as based on strong nebular emission lines (e.g., high $\text{EW}(\text{H}\beta) > 250 \text{ \AA}$, Izotov et al. 2020, 2024; Jaskot et al. 2019; Yang et al. 2017). The rest of the scenarios involving the lack of CRs (IC/synchrotron losses, CR escape etc.) would lead to a significant break at high frequencies (Klein et al. 2018). We do not observe such a break in the radio-SED of xSFGs in our sample. Indeed, J150934+373146 is an exception having the highest non-thermal fraction, which possibly has a more complex formation scenario due to a merger with another dwarf galaxy as argued by Dutta et al. (2024).

In summary, xSFGs lack a significant amount of non-thermal emission as they are young systems lacking a significant population of CRs which are accelerated in SNe explosions. This would suggest that feedback from SNe and CRs is not dominant in these galaxies. Thus radiation feedback might be important in such metal-poor starbursts (e.g., Jecmen & Oey 2023).

4.2. Dependence of LyC escape fraction on radio spectral index

Bait et al. (2024) using RC observations of a sub-sample of LzLCS sources from Flury et al. (2022a), showed that the radio spectral index measured between the VLA C- and S-bands ($\alpha_{6\text{GHz}}^{3\text{GHz}}$) correlates with the observed $f_{\text{esc}}^{\text{LyC}}$. We refer to this as the $f_{\text{esc}}^{\text{LyC}}-\alpha_{\text{high}}^{\text{low}}$ dependence hereon. Here we measure the radio spectral index ($\alpha_{\text{high}}^{\text{low}}$) for our detection sample of xSFGs and compare it with the indirectly estimated $f_{\text{esc}}^{\text{LyC}}$ in Figure 4. The $\alpha_{\text{high}}^{\text{low}}$ for different sources is measured at several GHz frequencies which show detection. In particular, we use X- and C-bands for J0159+0751 and J160810+352809, Ku- and X-bands for J1355+4651, and C- and S-bands for J150934+373146. The $f_{\text{esc}}^{\text{LyC}}$ is indirectly estimated using the empirical relation between the Ly α velocity peak separation (V_{sep}) and $f_{\text{esc}}^{\text{LyC}}$ from Izotov et al. (2018b) and are taken directly from Izotov et al. (2020, 2024). For J150934+373146 and J160810+352809, we use the V_{sep} values from Jaskot et al. (2019) to estimate the $f_{\text{esc}}^{\text{LyC}}$. The $f_{\text{esc}}^{\text{LyC}}$ values for LzLCS sources are taken from Flury et al. (2022a) and Saldana-Lopez et al. (2022) which are measured using the ‘‘UV-fit method’’ from HST/COS observations. And the $\alpha_{\text{high}}^{\text{low}}$ is measured between the VLA C- and S-bands taken from Bait et al. (2024). We also overplot in Figure 4 two nearby weak leakers, Haro 11 and Tol 1247 - 232 (see Bait et al. 2024, for references). The two horizontal dashed lines split the sources in three broad categories: strong leakers ($f_{\text{esc}}^{\text{LyC}} > 0.1$), weak leakers ($0.01 < f_{\text{esc}}^{\text{LyC}} < 0.1$), and non-leakers ($f_{\text{esc}}^{\text{LyC}} < 0.01$). The vertical dashed line represents the $\alpha_{6\text{GHz}}^{3\text{GHz}}$ for a simple radio-SED (Simple Model) with $f_{1\text{GHz}}^{\text{h}} = 0.1$ and $\alpha_{\text{nth}} = -0.8$. We generally refer to sources with $\alpha_{\text{high}}^{\text{low}} > -0.64$ as flat spectrum and $\alpha_{\text{high}}^{\text{low}} < -0.64$ as steep spectrum. Note that for J1355+4651, the data point exactly falls on another strong leaker source from the LzLCS sample.

Most xSFGs in our sample, except for J150934+373146, are likely strong LyC leakers and possess a flat radio spectrum, as seen in Figure 4. J150934+373146 is the only source which has

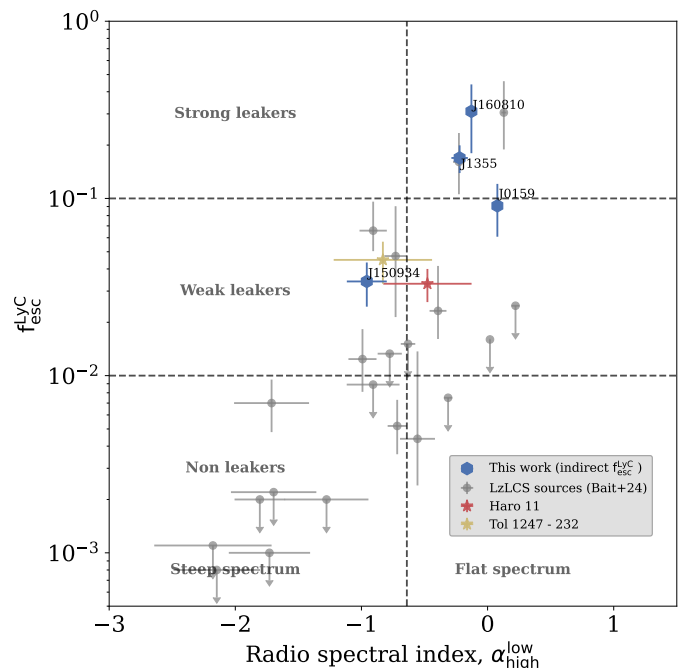


Fig. 4: Dependence of $f_{\text{esc}}^{\text{LyC}}$ on the radio spectral index, $\alpha_{\text{high}}^{\text{low}}$. xSFGs from this paper are shown in blue hexagons. The sub-sample of sources with VLA RC observations from Bait et al. (2024) are shown in grey circles, along with Haro 11 (red star) and Tol 1247 - 232 (yellow star). Here the $f_{\text{esc}}^{\text{LyC}}$ is measured directly using the HST/COS observations and the $\alpha_{\text{high}}^{\text{low}}$ is measured from observations in the C- and S-bands. For our sample of xSFGs the $f_{\text{esc}}^{\text{LyC}}$ is estimated indirectly using the empirical relation between V_{sep} and $f_{\text{esc}}^{\text{LyC}}$ from Izotov et al. (2018b). The $\alpha_{\text{high}}^{\text{low}}$ is measured at GHz frequencies which show a detection (see text for details). The two horizontal dashed lines demarcate the regions termed as strong-, weak- and non-leakers. The vertical dashed line represents $\alpha_{6\text{GHz}}^{3\text{GHz}} = -0.64$, corresponding to Simple Model, with $f_{1\text{GHz}}^{\text{h}} = 0.1$ and $\alpha_{\text{nth}} = -0.8$.

a steeper radio spectrum and is also a likely weak leaker. Taken together we observe that strong leakers are generally described by a flat radio spectrum at GHz frequencies. On the contrary, not all flat spectrum sources show strong LyC leakage, as we observe a few outliers from the LzLCS sample. Moreover, sources with steep spectrum are either weak- or non-leakers. Quite remarkably that our xSFGs with higher O_{32} values are less metal enriched (see Figure 5 for a comparison between O_{32} and metallicity) and also span a lower stellar mass range ($M_*/M_{\odot} \leq 10^8$) than LzLCS sources, follow the same $f_{\text{esc}}^{\text{LyC}}-\alpha_{\text{high}}^{\text{low}}$ dependence. We caution that the $f_{\text{esc}}^{\text{LyC}}$ for xSFGs is indirectly measured and can be uncertain. Thus, there is tentative evidence that the $f_{\text{esc}}^{\text{LyC}}-\alpha_{\text{high}}^{\text{low}}$ dependence holds independently of the stellar mass, metallicity and O_{32} ratio for compact star-forming galaxies. Future RC observations particularly focused on strong leakers with direct $f_{\text{esc}}^{\text{LyC}}$ measurements are required to confirm the universality of the $f_{\text{esc}}^{\text{LyC}}-\alpha_{\text{high}}^{\text{low}}$ dependence.

Bait et al. (2024) argued that the $f_{\text{esc}}^{\text{LyC}}-\alpha_{\text{high}}^{\text{low}}$ correlation could be primarily driven by a combination of the age of the starburst and the density variation of the ISM. Since the radio spectral index is a proxy for the age of the starburst (Cannon & Skill-

man 2004; Hirashita & Hunt 2006), the youngest starbursts (ages < 5 Myrs) would lack significant non-thermal emission (due to pre-SNe stellar populations) and thus they will have a flat radio spectrum. Additionally, if the source is compact, a large cluster of young stars would be packed in a small region thus boosting the ionized gas density ($N_e \gtrsim 10^3 \text{ cm}^{-3}$). Since the EM is strongly dependent on N_e ⁸, this leads to a high EM (in the range of $\sim 10^{7-8} \text{ pc cm}^{-6}$, see Hirashita & Hunt 2006, for a detailed model). Such high EMs are typically a sign of a dominance of young massive star clusters (YMCs; see Inoguchi et al. 2024, for a simulation study) in the ISM. Thus the radio free-free emission under such conditions would be optically thick at GHz frequencies (e.g., Johnson & Kobulnicky 2003; Hunt et al. 2004), further leading to a flat/rising radio spectrum associated with a FFA component (see also Hirashita & Hunt 2006; Bait et al. 2024, for a discussion on this).

Based on our study here, we observe a direct evidence for such a thermally dominated radio-SED which is optically thick at GHz frequencies (see Section 3.1) for our xSFGs (except in J150934+373146). This suggests that strong leakers possess a dominant population of YMCs in their HII regions. YMCs can boost the star-formation efficiency (SFE; Fall et al. 2010; Menon et al. 2024) thus leading to a paucity of neutral/ molecular gas thus opening channels for LyC photons to escape (Marques-Chaves et al. 2024). Such conditions can thus lead to both efficient production and escape of ionizing photons. Overall, this can explain the flat/rising radio spectrum of strong LyC leakers.

For relatively older starbursts (5 – 10 Myrs), where the radio free-free emission is optically thin and SNe explosions have accelerated the CR electrons producing a significant amount of non-thermal emission, the radio spectra are steeper. Moreover, in a relatively older starburst pressure-driven expansion of the HII region would lead to a lower EM (Hirashita & Hunt 2006), reducing the effect of flattening of the radio spectra due to FFA. Such conditions in the ISM would in general lead to a weaker LyC leakage, as observed in J150934+373146 which has a steep radio spectrum, with a $\nu_l < 1$ GHz and low $f_{\text{esc}}^{\text{LyC}}$ ($< 10\%$). Finally, Farcy et al. (2022) using radiation-magnetohydrodynamics simulations of disc galaxies find that the CR feedback overall leads to a smooth ISM filling it with denser gas. This overall leads to a lower $f_{\text{esc}}^{\text{LyC}}$ from galaxies. Thus the mere presence (lack) of CRs in weak/non-leakers (strong leakers) could also drive the $f_{\text{esc}}^{\text{LyC}} - \alpha_{\text{high}}^{\text{low}}$ dependence and explain its possible existence over a wide stellar mass range ($\log M_*/M_\odot = 6 - 11$). More work is needed on both the observation and modelling front to understand the exact physical mechanism(s) responsible for the $f_{\text{esc}}^{\text{LyC}} - \alpha_{\text{high}}^{\text{low}}$ dependence.

4.3. Relations between $\alpha_{6\text{GHz}}^{3\text{GHz}}$, ionization state and metallicity

High values of O_{32} ratio in galaxies could be associated with low-metallicity, high ionization parameter or the presence of density bounded HII regions (Jaskot & Oey 2013; Nakajima & Ouchi 2014). A high O_{32} ratio is found to be a necessary but not a sufficient condition for high $f_{\text{esc}}^{\text{LyC}}$ in galaxies (Izotov et al. 2018b; Jaskot et al. 2019; Nakajima et al. 2020; Flury et al. 2022b). Thus we investigate if the $f_{\text{esc}}^{\text{LyC}} - \alpha_{\text{high}}^{\text{low}}$ dependence could be driven by the dependence of $\alpha_{\text{high}}^{\text{low}}$ on O_{32} or metallicity.

⁸ $EM \propto N_e^2 L$, where L is the size of the emitting region, usually in the range of 10-100 pc (Hirashita & Hunt 2006).

The dependences between $O_{32} - \alpha_{\text{high}}^{\text{low}}$ and metallicity- $\alpha_{\text{high}}^{\text{low}}$ are presented in the left- and right-panel respectively of Figure 5 for xSFGs (in triangles). Such relations were studied by Bait et al. (2024) for a sub-sample of LzLCS sources which are shown in filled circles. This sub-sample lacked sources with very high O_{32} , which is covered by our xSFGs sample. We draw coloured circles around these points differentiating them in three categories: strong- (blue circles), weak- (orange circles) and non-leakers (red circles). Note that although J0159+0751 is classified as a weak-leaker, its $f_{\text{esc}}^{\text{LyC}}$ indirectly derived from the V_{sep} is $\sim 9.1\%$, thus very close to a strong leaker. Overall, we extend the positive correlation between O_{32} and $\alpha_{\text{high}}^{\text{low}}$ found by Bait et al. (2024) for the LzLCS sources, to the highest O_{32} ratios (> 10). And indeed as previously found the $f_{\text{esc}}^{\text{LyC}}$ generally increases with increasing O_{32} ratio (e.g., Izotov et al. 2018b). We also observe several outliers to this trend, wherein the flat spectrum sources have a range of O_{32} (and $f_{\text{esc}}^{\text{LyC}}$ values). The dependence of metallicity on $\alpha_{\text{high}}^{\text{low}}$ is not so tight. We do observe that the high metallicity sources from LzLCS have steep spectra (and low $f_{\text{esc}}^{\text{LyC}}$), although the flat radio spectrum sources are a mixed population. Thus as previously discussed, not all flat spectrum radio sources have high $f_{\text{esc}}^{\text{LyC}}$ (or high O_{32} /low-metallicity). Similar to the O_{32} ratio, it appears that a flat radio spectrum is a necessary but not a sufficient condition for strong LyC leakage from galaxies.

Based on the finding that not all high O_{32} ratio sources have high $f_{\text{esc}}^{\text{LyC}}$, several studies have suggested that there could be additional physical properties which govern LyC leakage from galaxies, with the viewing angle being a likely possibility (e.g., Izotov et al. 2018b; Jaskot et al. 2019; Nakajima et al. 2020; Katz et al. 2020; Bassett et al. 2019). In our xSFGs, we have such an example of J150934+373146, which has a high O_{32} value (> 10), and low metallicity comparable for instance to J160810+352809. Yet, their $f_{\text{esc}}^{\text{LyC}}$ values differ by an order of magnitude. However, we notice that their $\alpha_{\text{high}}^{\text{low}}$ values vary considerably and can be used to predict their indirect $f_{\text{esc}}^{\text{LyC}}$ values better (see Figure 4). On the other side, we also have sources from the LzLCS sample with low O_{32} that are strong leakers. Here again, such strong leakers have flat $\alpha_{\text{high}}^{\text{low}}$. Thus it appears that strong LyC leaking galaxies possess a flatter radio spectrum. Certainly, more data is needed to confirm if $\alpha_{\text{high}}^{\text{low}}$ could be a primary parameter governing LyC escape in the strongest leakers. If true, this along with the overall correlation between $\alpha_{\text{high}}^{\text{low}}$ and $f_{\text{esc}}^{\text{LyC}}$, and the fact that the $\alpha_{\text{high}}^{\text{low}}$ is a spatially averaged property could suggest that at least to a first order the orientation might not be a primary driver of $f_{\text{esc}}^{\text{LyC}}$ (see Bait et al. 2024, for a more detailed discussion). More importantly, the presence of a flat radio spectrum in strong leakers would suggest a lack of SNe in these systems, and consequently a lack of SNe feedback thus supporting theoretical models on metal-poor starbursts (Jecmen & Oey 2023). Thus other modes of feedback (e.g., radiation driven feedback) might be more important in leading to strong LyC leakage (see also Carr et al. 2024; Flury et al. 2024).

In summary, estimating $f_{\text{esc}}^{\text{LyC}}$ from galaxies is a multi-variate problem (e.g., Flury et al. 2022b; Jaskot et al. 2024), and along with the O_{32} ratio, metallicity, dust content and other physical properties, the radio spectral index can play an important role.

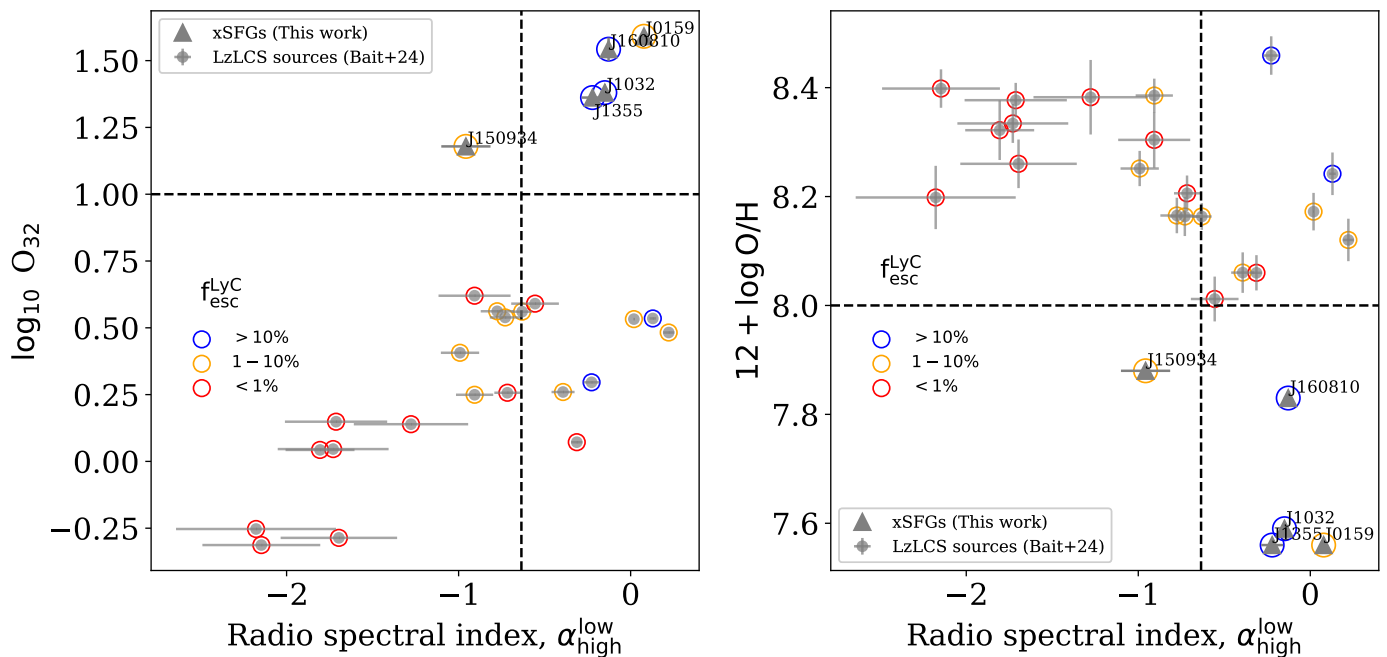


Fig. 5: Relations between O_{32} ratio and metallicity ($12 + \log O/H$) with radio spectral index for xSFGs (grey triangles). We show the LzLCS sources with RC measurements from Bait et al. (2024) (grey circles). Around each source we draw circles in blue ($f_{\text{esc}}^{\text{LyC}} > 10\%$), yellow ($f_{\text{esc}}^{\text{LyC}} = 1 - 10\%$) and red ($f_{\text{esc}}^{\text{LyC}} < 1\%$). See Figure 4 and text for details on how the $f_{\text{esc}}^{\text{LyC}}$ values are derived.

4.4. Overall implications from the radio-SED of xSFGs on reionization and high- z galaxies found with JWST

The radio-SED of several xSFGs is found to be thermally dominated along with a turnover at GHz frequencies owing to FFA. These radio-SEDs are akin to those found in ultracompact and hyper-compact HII regions in our Galaxy (Wood & Churchwell 1989; Yang et al. 2021; Patel et al. 2024). The presence of FFA at GHz frequencies is predicted to be a strong observational signature for the presence of YMCs from simulations (Inoguchi et al. 2024).

Thus our study provides a strong evidence for a picture wherein the extreme star-forming complexes in xSFGs are dominated by YMC(s) with pre-SNe stellar population (inferred from their thermal radio spectra). This leads to a high star-formation rate surface density together with a lack of SNe feedback which boosts the star-formation efficiency (SFE) (Fall et al. 2010; Menon et al. 2024) and can explain their extreme star-formation properties (Jecmen & Oey 2023; Marques-Chaves et al. 2024). Such a high SFE can lead to a lack of gas in such galaxies. This can explain the lack of HII detections in low- z green-pea/blueberry galaxies with high O_{32} ratio (Kanekar et al. 2021; Chandola et al. 2024) and the spatial offset between HII and peak of the SF, e.g., in J150934+373146 (Dutta et al. 2024). Together these effects lead to conditions which are suitable for a significant escape of LyC photons (Marques-Chaves et al. 2024; Menon et al. 2024).

Since xSFGs are excellent analogues of high- z galaxies (e.g., Schaerer et al. 2016, 2022; Rhoads et al. 2023), this suggests that the very high- z ($z \geq 6$) galaxies found by JWST might also possess a dominant population of YMCs in their HII regions. Indeed several studies find a dominance of such very dense starclusters in high- z JWST galaxies (Vanzella et al. 2023; Adamo et al. 2024; Messa et al. 2024; Fujimoto et al. 2024). Consequently,

these galaxies are expected to be strong LyC leakers and major contributors to reionization.

Finally, our radio-SED study suggests that future deep and ultra-deep radio surveys targeting high- z JWST galaxies with the SKA and ngVLA need to be sensitive to the free-free emission from these galaxies as they are expected to lack a dominant fraction of non-thermal emission.

5. Conclusions

We present new radio continuum observations of low- z xSFGs using the uGMRT, VLA and archival LOFAR telescope to study their radio-SED. xSFGs are a population of rare metal-poor ($12 + \log O/H < 8.0$), compact starburst galaxies at low- z . Using various indicators they are found to be excellent analogues of high- z ($z > 6$) galaxies found with JWST. We mapped the radio-SED in a wide frequency range from ~ 1 to 15 GHz (with a lower limit of 150 MHz for a few sources), to gain novel insights on the nature of extreme star-formation properties and the escape of LyC from these galaxies.

Our main results can be summarized as follows:

1. The radio-SEDs of xSFGs are generally flat between 6-15 GHz and thus are dominated by free-free emission, and showing a strong evidence for FFA with a turnover in the range 2-10 GHz (Figure 1). The estimated EM is very high in the range of $\sim 10^{7-9}$ pc cm $^{-6}$. This suggests that the star-formation is dominated by YMCs and pre-SNe stellar population. This explains the lack of non-thermal emission found in previous studies (Sec. 4.1) and their extreme properties (Sec. 4.4).
2. J150934+373146 has a complex radio-SED. It is steep at < 10 GHz with a turnover at ~ 400 MHz. At high frequencies (> 10 GHz) it shows a break and is flatter compared to that below 10 GHz (Figure 1 bottom panel).

3. We compared the free-free emission from 10 GHz radio flux with that expected from the observed optical emission line ($H\beta$) and find evidence for dust in several xSFGs. In a few xSFGs correcting for this dust using Balmer decrement does not account all the dust, thus suggesting a small amount of ionizing radiation emitted by the galaxy but not visible in the Balmer lines (Figure. 2).
4. Using indirect estimates of $f_{\text{esc}}^{\text{LyC}}$ in xSFGs, we confirmed the relation between $\alpha_{6\text{GHz}}^{3\text{GHz}}$ and $f_{\text{esc}}^{\text{LyC}}$ from Bait et al. (2024), particularly for strong leakers (Figure. 4). This suggests that most strong leakers lack SNe feedback and their SF is dominated by YMCs. Other modes of feedback, for example radiation driven mode might be more important for LyC leakage.
5. We also extended the previously found empirical relation between $\alpha_{6\text{GHz}}^{3\text{GHz}}$ and O_{32} ratio to high values of O_{32} (Figure 5).
6. Since xSFGs are excellent analogues of high- z galaxies, our study highlights the role of YMCs in explaining several extreme star-formation properties observed in recent JWST observations and can also lead to high LyC escape.

Acknowledgements. O. Bait (OB) is supported by the *AstroSignals* Sinergia Project funded by the Swiss National Science Foundation. OB would like to thank Heidi Medlin for help with the VLA scheduling. We thank the staff of the GMRT who have made these observations possible. GMRT is run by the National Center for Radio Astrophysics (NCRA) of the Tata Institute of Fundamental Research. OB would also like to thank NCRA for hosting him where part of this work was completed. Y.I. acknowledges support from the National Academy of Sciences of Ukraine (Project No. 0123U102248) and from the Simons Foundation. LOFAR is the Low Frequency Array designed and constructed by ASTRON. It has observing, data processing, and data storage facilities in several countries, which are owned by various parties (each with their own funding sources), and which are collectively operated by the ILT foundation under a joint scientific policy. The ILT resources have benefited from the following recent major funding sources: CNRS-INSU, Observatoire de Paris and Université d'Orléans, France; BMBF, MIWF-NRW, MPG, Germany; Science Foundation Ireland (SFI), Department of Business, Enterprise and Innovation (DBEI), Ireland; NWO, The Netherlands; The Science and Technology Facilities Council, UK; Ministry of Science and Higher Education, Poland; The Istituto Nazionale di Astrofisica (INAF), Italy. This research made use of the Dutch national e-infrastructure with support of the SURF Cooperative (e-infra 180169) and the LOFAR e-infra group. The Jülich LOFAR Long Term Archive and the German LOFAR network are both coordinated and operated by the Jülich Supercomputing Centre (JSC), and computing resources on the supercomputer JUWELS at JSC were provided by the Gauss Centre for Supercomputing e.V. (grant CHTB00) through the John von Neumann Institute for Computing (NIC). This research made use of the University of Hertfordshire high-performance computing facility and the LOFAR-UK computing facility located at the University of Hertfordshire and supported by STFC [ST/P000096/1], and of the Italian LOFAR IT computing infrastructure supported and operated by INAF, and by the Physics Department of Turin university (under an agreement with Consorzio Interuniversitario per la Fisica Spaziale) at the C3S Supercomputing Centre, Italy.

References

Adamo, A., Bradley, L. D., Vanzella, E., et al. 2024, *Nature*, 632, 513
Atek, H., Labbé, I., Furtak, L. J., et al. 2024, *Nature*, 626, 975
Atek, H., Richard, J., Jauzac, M., et al. 2015, *ApJ*, 814, 69
Bait, O., Borthakur, S., Schaerer, D., et al. 2024, *A&A*, 688, A198
Bassett, R., Ryan-Weber, E. V., Cooke, J., et al. 2019, *MNRAS*, 483, 5223
Borkar, A., Grossová, R., Svoboda, J., et al. 2024, *A&A*, 687, A137
Borthakur, S., Heckman, T. M., Leitherer, C., & Overzier, R. A. 2014, *Science*, 346, 216
Bouwens, R. J., Illingworth, G. D., Oesch, P. A., et al. 2015, *ApJ*, 811, 140
Cannon, J. M. & Skillman, E. D. 2004, *ApJ*, 610, 772
Cardamone, C., Schawinski, K., Sarzi, M., et al. 2009, *MNRAS*, 399, 1191
Cardelli, J. A., Clayton, G. C., & Mathis, J. S. 1989, *ApJ*, 345, 245
Carilli, C. L., Lee, N., Capak, P., et al. 2008, *ApJ*, 689, 883
Carr, C. A., Cen, R., Scarlata, C., et al. 2024, arXiv e-prints, arXiv:2409.05180
Chakraborti, S., Yadav, N., Cardamone, C., & Ray, A. 2012, *ApJ*, 746, L6
Chandola, Y., Tsai, C.-W., Saikia, D. J., et al. 2024, arXiv e-prints, arXiv:2411.13527
Chyży, K. T., Jurusik, W., Piotrowska, J., et al. 2018, *A&A*, 619, A36
Clemens, M. S., Scaife, A., Vega, O., & Bressan, A. 2010, *MNRAS*, 405, 887

Condon, J. J. 1992, *ARA&A*, 30, 575
Condon, J. J. & Ransom, S. M. 2016, *Essential Radio Astronomy*
Deeg, H.-J., Brinks, E., Duric, N., Klein, U., & Skillman, E. 1993, *ApJ*, 410, 626
Dey, S., Goyal, A., Małek, K., & Díaz-Santos, T. 2024, *ApJ*, 966, 61
Dutta, S., Bera, A., Bait, O., et al. 2024, *MNRAS*[arXiv:2406.08341]
Emsley, R., Stark, D. P., Whitler, L., et al. 2023, *MNRAS*, 524, 2312
Fall, S. M., Krumholz, M. R., & Matzner, C. D. 2010, *ApJ*, 710, L142
Farcy, M., Rosdahl, J., Dubois, Y., Blaizot, J., & Martin-Alvarez, S. 2022, *MNRAS*, 513, 5000
Flury, S. R., Jaskot, A. E., Ferguson, H. C., et al. 2022a, *ApJS*, 260, 1
Flury, S. R., Jaskot, A. E., Ferguson, H. C., et al. 2022b, *ApJ*, 930, 126
Flury, S. R., Jaskot, A. E., Saldana-Lopez, A., et al. 2024, arXiv e-prints, arXiv:2409.12118
Fujimoto, S., Arrabal Haro, P., Dickinson, M., et al. 2023, *ApJ*, 949, L25
Fujimoto, S., Ouchi, M., Kohno, K., et al. 2024, arXiv e-prints, arXiv:2402.18543
Galvin, T. J., Seymour, N., Marvil, J., et al. 2018, *MNRAS*, 474, 779
Greis, S. M. L., Stanway, E. R., Levan, A. J., Davies, L. J. M., & Eldridge, J. J. 2017, *MNRAS*, 470, 489
Grundy, J. A., Seymour, N., Wong, O. I., et al. 2024, arXiv e-prints, arXiv:2412.03143
Hayes, M., Östlin, G., Atek, H., et al. 2007, *MNRAS*, 382, 1465
Hirashita, H. & Hunt, L. K. 2006, *A&A*, 460, 67
Hunt, L. K., Dyer, K. K., Thuan, T. X., & Ulvestad, J. S. 2004, *ApJ*, 606, 853
Inoguchi, M., Hosokawa, T., Fukushima, H., et al. 2024, *MNRAS*, 527, 3612
Inoue, A. K., Shimizu, I., Iwata, I., & Tanaka, M. 2014, *MNRAS*, 442, 1805
Izotov, Y. I., Guseva, N. G., Fricke, K. J., & Henkel, C. 2016a, *MNRAS*, 462, 4427
Izotov, Y. I., Guseva, N. G., Fricke, K. J., Henkel, C., & Schaerer, D. 2017a, *MNRAS*, 467, 4118
Izotov, Y. I., Guseva, N. G., Fricke, K. J., et al. 2021a, *A&A*, 646, A138
Izotov, Y. I., Guseva, N. G., & Thuan, T. X. 2011, *ApJ*, 728, 161
Izotov, Y. I., Orlitová, I., Schaerer, D., et al. 2016b, *Nature*, 529, 178
Izotov, Y. I., Schaerer, D., Thuan, T. X., et al. 2016c, *MNRAS*, 461, 3683
Izotov, Y. I., Schaerer, D., Worseck, G., et al. 2018a, *MNRAS*, 474, 4514
Izotov, Y. I., Schaerer, D., Worseck, G., et al. 2020, *MNRAS*, 491, 4680
Izotov, Y. I., Thuan, T. X., & Guseva, N. G. 2017b, *MNRAS*, 471, 548
Izotov, Y. I., Thuan, T. X., Guseva, N. G., et al. 2024, *MNRAS*, 527, 281
Izotov, Y. I., Worseck, G., Schaerer, D., et al. 2021b, *MNRAS*, 503, 1734
Izotov, Y. I., Worseck, G., Schaerer, D., et al. 2018b, *MNRAS*, 478, 4851
Jaskot, A. E., Dowd, T., Oey, M. S., Scarlata, C., & McKinney, J. 2019, *ApJ*, 885, 96
Jaskot, A. E. & Oey, M. S. 2013, *ApJ*, 766, 91
Jaskot, A. E., Silveyra, A. C., Plantinga, A., et al. 2024, arXiv e-prints, arXiv:2406.10171
Jecmen, M. C. & Oey, M. S. 2023, *ApJ*, 958, 149
Johnson, K. E. & Kobulnicky, H. A. 2003, *ApJ*, 597, 923
Jones, T., Sanders, R., Roberts-Borsani, G., et al. 2020, *ApJ*, 903, 150
Kanekar, N., Ghosh, T., Rhoads, J., et al. 2021, *ApJ*, 913, L15
Katz, H., Durovčíková, D., Kimm, T., et al. 2020, *MNRAS*, 498, 164
Kennicutt, R. C. & Evans, N. J. 2012, *ARA&A*, 50, 531
Kennicutt, Jr., R. C. 1998, *ARA&A*, 36, 189
Klein, U., Lisenfeld, U., & Verley, S. 2018, *A&A*, 611, A55
Klein, U., Weiland, H., & Brinks, E. 1991, *A&A*, 246, 323
Kobulnicky, H. A. & Johnson, K. E. 1999, *ApJ*, 527, 154
Langeroodi, D., Hjorth, J., Chen, W., et al. 2023, *ApJ*, 957, 39
Lisenfeld, U., Wilding, T. W., Pooley, G. G., & Alexander, P. 2004, *MNRAS*, 349, 1335
Marques-Chaves, R., Schaerer, D., Vanzella, E., et al. 2024, arXiv e-prints, arXiv:2407.18804
Mascia, S., Pentericci, L., Calabrò, A., et al. 2024, *A&A*, 685, A3
McMullin, J. P., Waters, B., Schiebel, D., Young, W., & Golap, K. 2007, in *Astronomical data analysis software and systems XVI*, Vol. 376, 127
Melnick, J., Heydari-Malayeri, M., & Leisy, P. 1992, *A&A*, 253, 16
Menon, S. H., Burkhart, B., Somerville, R. S., Thompson, T. A., & Sternberg, A. 2024, arXiv e-prints, arXiv:2408.14591
Messa, M., Vanzella, E., Loiacono, F., et al. 2024, arXiv e-prints, arXiv:2407.20331
Mohan, N. & Rafferty, D. 2015, *PyBDSF: Python Blob Detection and Source Finder*, *Astrophysics Source Code Library*, record ascl:1502.007
Murphy, E. J., Condon, J. J., Schinnerer, E., et al. 2011, *ApJ*, 737, 67
Nakajima, K., Ellis, R. S., Robertson, B. E., Tang, M., & Stark, D. P. 2020, *ApJ*, 889, 161
Nakajima, K. & Ouchi, M. 2014, *MNRAS*, 442, 900
Niklas, S., Klein, U., & Wielebinski, R. 1997, *A&A*, 322, 19
Ouchi, M., Mobasher, B., Shimasaku, K., et al. 2009, *ApJ*, 706, 1136
Patel, A. L., Urquhart, J. S., Yang, A. Y., et al. 2024, *MNRAS*, 533, 2005
Paudel, S., Yoon, S.-J., Bait, O., et al. 2023, *ApJ*, 951, L36
Ramya, S., Kantharia, N. G., & Prabhu, T. P. 2011, *ApJ*, 728, 124
Rau, U. & Cornwell, T. J. 2011, *A&A*, 532, A71

- Rhoads, J. E., Wold, I. G. B., Harish, S., et al. 2023, *ApJ*, 942, L14
- Robertson, B. E., Ellis, R. S., Furlanetto, S. R., & Dunlop, J. S. 2015, *ApJ*, 802, L19
- Saldana-Lopez, A., Schaerer, D., Chisholm, J., et al. 2022, *A&A*, 663, A59
- Saxena, A., Bunker, A. J., Jones, G. C., et al. 2024, *A&A*, 684, A84
- Schaerer, D., Izotov, Y. I., Verhamme, A., et al. 2016, *A&A*, 591, L8
- Schaerer, D., Marques-Chaves, R., Barrufet, L., et al. 2022, *A&A*, 665, L4
- Sebastian, B. & Bait, O. 2019, *ApJ*, 882, L19
- Shimwell, T. W., Hardcastle, M. J., Tasse, C., et al. 2022, *A&A*, 659, A1
- Shimwell, T. W., Röttgering, H. J. A., Best, P. N., et al. 2017, *A&A*, 598, A104
- Simmonds, C., Tacchella, S., Hainline, K., et al. 2024, arXiv e-prints, arXiv:2409.01286
- Simmonds, C., Tacchella, S., Maseda, M., et al. 2023, *MNRAS*, 523, 5468
- Tabatabaei, F. S., Schinnerer, E., Krause, M., et al. 2017, *ApJ*, 836, 185
- THE CASA TEAM, Bean, B., Bhatnagar, S., et al. 2022, arXiv e-prints, arXiv:2210.02276
- Thuan, T. X., Hibbard, J. E., & Lévrier, F. 2004, *AJ*, 128, 617
- Topping, M. W., Stark, D. P., Senchyna, P., et al. 2024, *MNRAS*, 529, 3301
- Vanzella, E., Claeysens, A., Welch, B., et al. 2023, *ApJ*, 945, 53
- Verhamme, A., Orlitová, I., Schaerer, D., & Hayes, M. 2015, *A&A*, 578, A7
- Williams, H., Kelly, P. L., Chen, W., et al. 2023, *Science*, 380, 416
- Wood, D. O. S. & Churchwell, E. 1989, *ApJS*, 69, 831
- Xu, X., Henry, A., Heckman, T., et al. 2023, *ApJ*, 943, 94
- Yang, A. Y., Urquhart, J. S., Thompson, M. A., et al. 2021, *A&A*, 645, A110
- Yang, H., Malhotra, S., Rhoads, J. E., & Wang, J. 2017, *ApJ*, 847, 38

Appendix A: Deriving the radio-based $\text{Flux}_{\text{H}\beta}^{\text{Exp}}$ flux density

We derive the expected H β line flux density from radio ($\text{Flux}_{\text{H}\beta}^{\text{Exp}}$) following H04 (see their Appendix Eq. A10) which relates the radio-derived thermal flux density and the H β line flux density. This relation has been found to be better applicable for low-metallicity HII with high electron temperatures ($> 10,000$ K) which is the case for xSFGs. Here we also assumed a ionized Helium to Hydrogen ratio of 0.08 which is typical of low-metallicity environments (Melnick et al. 1992; Hunt et al. 2004). We used the T_e values from Izotov et al. (2020, 2024). For J150934+373146 and J160810+352809 we used a fixed value of 20,000 K.

We have used the observed high-frequency VLA 10 GHz (X-band) flux densities to derive $\text{Flux}_{\text{H}\beta}^{\text{Exp}}$. This is because for xSFGs we find that their entire radio-SED is significantly thermally dominant, thus further reducing any minor contribution from non-thermal emission. Further, we prefer the X-band since it has the largest coverage for our sample as opposed to the Ku-band (15 GHz).